

International Journal of Modern Physics E  
© World Scientific Publishing Company

## STUDY OF NEUTRON MAGIC DRIP-LINE NUCLEI WITHIN RELATIVISTIC MEAN-FIELD PLUS BCS APPROACH

G. SAXENA

*Department of Physics, Govt. Women Engineering College, Ajmer-305002, India \**  
*gauravphy@gmail.com*

D. SINGH

*Department of Physics, University of Rajasthan, Jaipur-302004, India*

M. KAUSHIK

*Department of Physics, University of Rajasthan, Jaipur-302004, India*

H. L. YADAV

*Department of Physics, Banaras Hindu University, Varanasi-221005, India*  
*hlyadavphysics@gmail.com*

H. TOKI

*Research Center for Nuclear Physics (RCNP), Osaka University, 10-1, Mihogaoka, Ibaraki,  
Osaka 567-0047, Japan*

Received Day Month Year  
Revised Day Month Year

Encouraged by the success of RMF+BCS approach for the description of the ground state properties of the chains of isotopes of proton magic nuclei with proton number  $Z=8, 20, 28, 50$  and  $82$  as well as those of proton sub-magic nuclei with  $Z=40$ , we have further employed it, in an analogous manner, for a detailed calculations of the ground state properties of the neutron magic isotones with neutron number  $N = 8, 20, 28, 50, 82$  and  $126$  as well as those of neutron sub-magic isotones with  $N = 40$  using the TMA force parameterizations in order to explore low lying resonance and other exotic phenomenon near drip-lines. The results of these calculations for wave-function, single particle pairing gaps etc. are presented here to demonstrate the general validity of our RMF+BCS approach. It is found that, in some of the proton-rich nuclei in the vicinity of the proton drip-line, the main contribution to the pairing correlations is provided by the low-lying resonant states, in addition to the contributions coming from the states close to the Fermi surface, which results extended proton drip-line for isotonic chain.

*Keywords:* Drip-line nuclei; Relativistic mean-field plus BCS approach; two proton sep-

\*Corresponding author

2 *G. Saxena, D. Singh, M. Kaushik, H. L. Yadav and H. Toki*

aration energy; Potential; Radial Wave function; Pairing energy; Pairing gap.

21.10.-k, 21.10.Ft, 21.10.Dr, 21.10.Gv, 21.10.-n, 21.60.Jz

## 1. Introduction

During the last few years, phenomenal advances in nuclear experimental techniques and the spectacular growth in accelerator and detection technology have led to the development of radioactive nuclear beams facilities around the world <sup>1,2,3,4,5,6,7</sup>. With these remarkable efforts it has been possible to study exotic nuclei in the region far from the line of  $\beta$ -stability in the nuclear chart. As far as theoretical studies are concern for these nuclei in neutron- and proton-rich side they have been mostly carried out within the framework of mean-field theories <sup>8,9,10,11,12,13</sup>, as well as employing their relativistic counterparts <sup>14-29</sup>. The effect of continuum on the pairing energy contribution within the HF+BCS+Resonant continuum approach has been calculated by Grasso *et al.* <sup>11</sup> and Sandulescu *et al.* <sup>12,13</sup>. Similarly, the effect of inclusion of positive energy resonant states on the pairing correlations has been investigated quite elaborately for the unstable nuclei by Yadav *et al.* <sup>28,29</sup> within the framework of relativistic mean-field (RMF) theory.

RMF approach has proved to be very crucial for the study of unstable nuclei near the drip-line because it provides the spin-orbit interaction in the entire mass region in a natural way <sup>14,15,16,17,18</sup>, and the single particle properties near the threshold are prone to large changes as compared to the case of deeply bound levels in the nuclear potential for drip-line nuclei. Indeed the RMF+BCS scheme <sup>29</sup> yields results which are in close agreement with the experimental data and with those of recent continuum relativistic Hartree-Bogoliubov (RCHB) and other similar mean-field calculations <sup>26,27</sup>.

In the present investigations we have further employed the relativistic mean-field plus BCS approach <sup>28,29,30,31,32</sup> to carry out a systematic study for the ground state properties of the entire chains of neutron magic nuclei represented by isotones of traditional neutron magic numbers  $N = 8, 20, 28, 50, 82$  and 126 as well as isotones of  $N = 40$ , considered to be neutron sub-magic <sup>33</sup>. These chains of magic isotones cover the different regions of the periodic table and their study is expected to provide further testing ground for the general validity of the RMF+BCS approach, including for the magic isotones in the region away from the line of  $\beta$ -stability up to the drip-lines. Additionally, these calculations are expected to shed light on the evolution of neutron and/or proton magicity as we move away from line of  $\beta$ -stability to approach the proton or neutron drip-line. This study of isotones will provide additional impetus on the recent developments on isotones <sup>34,35,36,37</sup>.

## 2. Relativistic Mean-Field Model

In our RMF approach we have used the model Lagrangian density with nonlinear terms both for the  $\sigma$  and  $\omega$  mesons. Our calculations are performed with the TMA parametrization as described in detail in Refs. 23, 28, 30, 31.

$$\begin{aligned}
 \mathcal{L} = & \bar{\psi}[\gamma^\mu \partial_\mu - M]\psi \\
 & + \frac{1}{2} \partial_\mu \sigma \partial^\mu \sigma - \frac{1}{2} m_\sigma^2 \sigma^2 - \frac{1}{3} g_2 \sigma^3 - \frac{1}{4} g_3 \sigma^4 - g_\sigma \bar{\psi} \sigma \psi \\
 & - \frac{1}{4} H_{\mu\nu} H^{\mu\nu} + \frac{1}{2} m_\omega^2 \omega_\mu \omega^\mu + \frac{1}{4} c_3 (\omega_\mu \omega^\mu)^2 - g_\omega \bar{\psi} \gamma^\mu \psi \omega_\mu \\
 & - \frac{1}{4} G_{\mu\nu}^a G^{a\mu\nu} + \frac{1}{2} m_\rho^2 \rho_\mu^a \rho^{a\mu} - g_\rho \bar{\psi} \gamma_\mu \tau^a \psi \rho^{\mu a} \\
 & - \frac{1}{4} F_{\mu\nu} F^{\mu\nu} - e \bar{\psi} \gamma_\mu \frac{(1 - \tau_3)}{2} A^\mu \psi ,
 \end{aligned} \tag{1}$$

where  $H$ ,  $G$  and  $F$  are field tensors for the vector fields and defined by

$$\begin{aligned}
 H_{\mu\nu} &= \partial_\mu \omega_\nu - \partial_\nu \omega_\mu \\
 G_{\mu\nu}^a &= \partial_\mu \rho_\nu^a - \partial_\nu \rho_\mu^a - 2g_\rho \epsilon^{abc} \rho_\mu^b \rho_\nu^c \\
 F_{\mu\nu} &= \partial_\mu A_\nu - \partial_\nu A_\mu ,
 \end{aligned}$$

and other symbols have their usual meaning. We perform a state dependent BCS calculations<sup>38,39</sup> on the basis of single-particle spectrum calculated by the RMF described above. The continuum is replaced by a set of positive energy states generated by enclosing the nucleus in a spherical box. Thus the gap equations have the standard form for all the single particle states, i.e.

$$\Delta_{j_1} = -\frac{1}{2} \frac{1}{\sqrt{2j_1+1}} \sum_{j_2} \frac{\langle (j_1^2) 0^+ | V | (j_2^2) 0^+ \rangle}{\sqrt{(\varepsilon_{j_2} - \lambda)^2 + \Delta_{j_2}^2}} \sqrt{2j_2+1} \Delta_{j_2} , \tag{2}$$

where  $\varepsilon_{j_2}$  are the single particle energies, and  $\lambda$  is the Fermi energy, whereas the particle number condition is given by  $\sum_j (2j+1)v_j^2 = N$ . A delta force i.e.,  $V = -V_0\delta(r)$  is used in the calculations for the pairing interaction, with the same strength  $V_0$  for both protons and neutrons. The value of this interaction strength  $V_0 = 350$  MeV fm<sup>3</sup> was determined in Ref. 28 by obtaining a best fit to the binding energy of Ni isotopes. We use the same value of  $V_0$  for our present studies of isotopes of other nuclei as well. Apart from its simplicity, the applicability and justification of using such a  $\delta$ -function form of interaction has been discussed in Refs. 8, 40, 41. The pairing matrix element for the  $\delta$ -function force is given by

$$\langle (j_1^2) 0^+ | V | (j_2^2) 0^+ \rangle = -\frac{V_0}{8\pi} \sqrt{(2j_1+1)(2j_2+1)} I_R , \tag{3}$$

where  $I_R$  is the radial integral with the form

$$I_R = \int dr \frac{1}{r^2} (G_{j_1}^* G_{j_2} + F_{j_1}^* F_{j_2})^2 \tag{4}$$

Here  $G_\alpha$  and  $F_\alpha$  denote the radial wave functions for the upper and lower components, respectively, of the nucleon wave function expressed as

$$\psi_\alpha = \frac{1}{r} \begin{pmatrix} i G_\alpha \mathcal{Y}_{j_\alpha l_\alpha m_\alpha} \\ F_\alpha \sigma \cdot \hat{r} \mathcal{Y}_{j_\alpha l_\alpha m_\alpha} \end{pmatrix} , \tag{5}$$

4 *G. Saxena, D. Singh, M. Kaushik, H. L. Yadav and H. Toki*

and satisfy the normalization condition

$$\int dr \{|G_\alpha|^2 + |F_\alpha|^2\} = 1 \quad (6)$$

In Eq. (5) the symbol  $\mathcal{Y}_{jlm}$  has been used for the standard spinor spherical harmonics with the phase  $i^l$ . The coupled field equations obtained from the Lagrangian density in (1) are finally reduced to a set of simple radial equations<sup>17,18</sup> which are solved self consistently along with the equations for the state dependent pairing gap  $\Delta_j$  and the total particle number  $N$  for a given nucleus.

The relativistic mean-field description has been extended for the deformed nuclei of axially symmetric shapes by Gambhir, Ring and their collaborators<sup>19,20</sup> using an expansion method. The treatment of pairing has been carried out in Ref. 32 using state dependent BCS method<sup>38</sup> as has been given by Yadav et al.<sup>28,29</sup> for the spherical case. For axially deformed nuclei the rotational symmetry is no more valid and the total angular momentum  $j$  is no longer a good quantum number. Nevertheless, the various densities still are invariant with respect to a rotation around the symmetry axis. Here we have taken the symmetry axis to be the  $z$ -axis. Following Gambhir *et al.*<sup>19,20</sup>, it is then convenient to employ the cylindrical coordinates.

The scalar, vector, isovector and charge densities, as in the spherical case, are expressed in terms of the spinor  $\pi_i$ , its conjugate  $\pi_i^+$ , operator  $\tau_3$  etc. These densities serve as sources for the fields  $\phi = \sigma, \omega^0, \rho^0$  and  $A^0$ , which are determined by the Klein-Gordon equation in cylindrical coordinates. Thus a set of coupled equations, namely the Dirac equation with potential terms for the nucleons and the Klein-Gordon type equations with sources for the mesons and the photon is obtained. These equations are solved self consistently. For this purpose, as described above, the well-tested basis expansion method<sup>42</sup> has been employed<sup>19,20</sup>. Using anisotropic (axially symmetric) harmonic oscillator potential the bases are generated. These bases are used to expand the upper and lower components of the nucleon spinors, the fields, the baryon currents and densities separately. In this expansion method the solution of the Klein-Gordon equation reduces to a set of inhomogeneous equations while the Dirac equation gets reduced to a symmetric matrix diagonalization problem. Solution of these equations provide the spinor fields, and the nucleon currents and densities (sources of the fields). From these fields all the relevant ground state nuclear properties are calculated. For further details of these formulations we refer the reader to Ref. 19, 20, 30, 32.

### 3. Results and Discussion

#### 3.1. $N = 28$ Isotones: A Representative Case of Neutron Magic Nuclei

It has been earlier demonstrated in the case of neutron-rich isotopes of proton magic nuclei<sup>29</sup> that the neutron resonant states lying near the Fermi level have their wave

functions mostly confined within the nuclear potential region. Consequently, these resonant states have properties akin to a bound state. This enables a resonant state to accommodate many more neutrons resulting in extremely neutron-rich bound nuclei. Accommodation of more neutrons in turn finally extends further the neutron drip-line. The present study of isotones is intended to demonstrate the persistence of this phenomenon in the case of neutron magic nuclei as well. Thus, in the case of neutron magic isotones the proton drip-line, instead of neutron drip-line, is found to be extended. However, in contrast to the neutron drip-line case of proton magic nuclei, here the effect of extending the proton drip-line is not seen to be pronounced. This is due to the disruptive effect of Coulomb forces which very much limit the number of protons being accommodated while keeping the isotonic nucleus bound.

Moreover, as per the definition of two proton (neutron) drip-lines the nuclei become unbound as soon as the two proton (neutron) separation energy approaches zero. However, some nuclei even with negative two proton separation energy may have finite life time due to the combined effect of Coulomb and centrifugal barriers. This life time may be large enough to allow even such a nucleus to be studied experimentally. This effect in combination with the resonant states phenomenon described above effectively further pushes the proton drip-line with nuclei having negative two proton separation energy.

The shell closures with pronounced gaps between shells in nuclei endow them with spherical shape. Consequently, the magic nuclei are characterized with zero deformation. In our systematic investigations we first carry out RMF+BCS calculations including the deformation degree of freedom (to be referred to throughout as deformed RMF+BCS) to establish whether the entire chain of magic isotones for a given neutron number is indeed spherical or not. It is gratifying to note that leaving aside a few exceptions away from the line of stability in the case of  $N = 40$  and also to some extent for the neutron-rich  $N = 28$  isotones, invariably the entire chain of nuclei shows negligible deformation, especially for  $N = 8, 20, 50, 82$  and  $126$  where entire chain shows zero deformation.

In the case of negligible/zero deformation, we take advantage of the RMF+BCS approach for spherical shapes (to be referred to throughout as spherical RMF+BCS) for the analysis of results in terms of spherical single particle wave functions and energy levels to make the discussion of shell closures and magicity more convenient and transparent. Also, behavior of the single particle states near the Fermi surface which in turn plays an important role near the drip-line can be easily understood. Moreover, within such a framework contributions of neutron and proton single particle states to the density profiles, pairing gaps, total pairing energy and separation energy which are also equally important in the study of exotic phenomena can be demonstrated with clarity. This approach indeed turns out to be very useful for the study of poorly understood exotic nuclei.

Our spherical RMF+BCS calculations have been performed with two different force parametrization, TMA and NL-SH<sup>23,25</sup> to check if the results have any

6 *G. Saxena, D. Singh, M. Kaushik, H. L. Yadav and H. Toki*

dependence on force parametrization. Details of our calculations show that the two interactions employed here produce very similar results. Therefore, unless required, in most of the cases we have presented the results obtained with the TMA force<sup>23</sup> only.

### 3.1.1. Proton-Rich Nucleus ${}^{58}_{30}\text{Zn}_{28}$ at the drip-line:

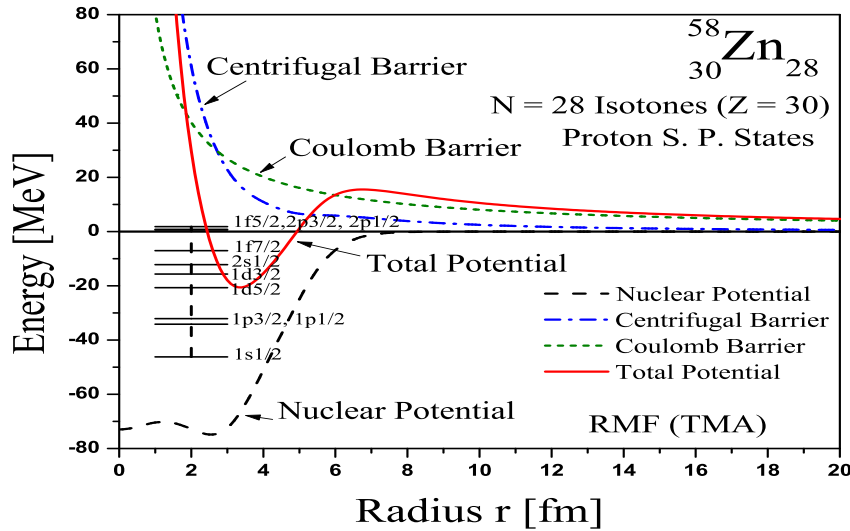


Fig. 1. The RMF potential energy (sum of the scalar and vector potentials), for the nucleus  ${}^{58}_{30}\text{Zn}_{28}$  as a function of radius is shown by the black long dashed line. The centrifugal barrier energy for proton resonant states  $1f_{5/2}$  and coulomb barrier are also shown in the figure by dot dashed blue line and dashed green line respectively. The red solid line represents total potential, the sum of RMF potential energy, the centrifugal barrier energy and the coulomb barrier. The figure also shows the energy spectrum of the proton single particle states lying close to the Fermi level and include both the bound and continuum states. The important resonant states  $1f_{5/2}$ ,  $2p_{3/2}$  and  $2p_{1/2}$  at 0.57, 0.84 and 1.82 MeV, respectively are also depicted in the figure.

In order to demonstrate our results for the proton-rich nucleus  ${}^{58}_{30}\text{Zn}_{28}$  of the  $N = 28$  isotonic chain, we have plotted in Fig. 1 the calculated RMF potential, a sum of scalar and vector potentials, along with the spectrum of the bound proton single particle states. Though this is a typical example of the proton-rich case, the main features of the potential, single particle spectrum and wave functions besides some finer details remain valid for all the isotones. The figure also shows the positive energy proton single particle states corresponding to the low-lying resonances  $1f_{5/2}$ ,  $2p_{3/2}$  and  $2p_{1/2}$  close to the Fermi surface. Amongst these, it is observed that

especially the resonant states play significant role in the binding of proton-rich isotone  $^{58}_{30}\text{Zn}_{28}$  through their contributions to the total pairing energy. In contrast to other states in the box, the respective position of the resonant  $1f_{5/2}$ ,  $2p_{3/2}$  and  $2p_{1/2}$  states is not much affected by changing the box radius around  $R = 30$  fm. For the purpose of illustration we have also depicted in Fig. 1 centrifugal barrier of  $1f_{5/2}$  states and coulomb barrier. The total mean-field potential, obtained by adding the centrifugal potential energy and coulomb barrier energy is also shown. It is evident from the figure that the total effective potential for the  $1f_{5/2}$  state including coulomb barrier, has an appreciable barrier for the trapping of waves to form a quasi-bound or resonant state. Such a meta-stable state remains mainly confined to the region of the potential well and the wave function exhibits characteristics similar to that of a bound state.

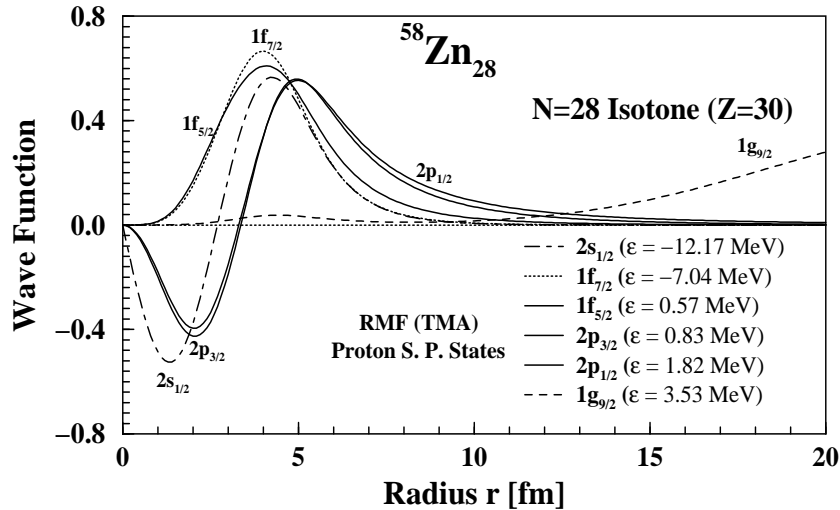


Fig. 2. Radial wave functions of a few representative proton single particle states with energy close to the Fermi surface for the nucleus  $^{58}_{30}\text{Zn}_{28}$ . The resonant states  $1f_{5/2}$ ,  $2p_{3/2}$  and  $2p_{1/2}$  at energies 0.57, 0.84 and 1.82 MeV, respectively, are shown by solid lines, while the bound  $2s_{1/2}$  state at -12.17 MeV, and  $1f_{7/2}$  state at -7.04 MeV are shown by long dashed and dotted lines. The continuum  $1g_{9/2}$  state at 3.53 MeV has been depicted by small dashed line. It is seen that the resonant states in the continuum have characteristics similar to the bound states and are confined within the potential region.

This is clearly observed in Fig. 2 which depicts the radial wave functions of some of the proton single particle states lying close to the Fermi surface with the proton Fermi energy being  $\lambda_p = -0.097$  MeV. These include the bound  $1f_{7/2}$  and  $2s_{1/2}$  states, in addition to the resonant  $1f_{5/2}$ ,  $2p_{3/2}$  and  $2p_{1/2}$  states. As an example of a non-resonant state, the figure also depicts a typical high lying continuum  $1g_{9/2}$  state at 3.53 MeV. The wave functions for the  $1f_{5/2}$ ,  $2p_{3/2}$  and  $2p_{1/2}$  states in Fig.

8 *G. Saxena, D. Singh, M. Kaushik, H. L. Yadav and H. Toki*

2 are clearly seen to be confined within a radial range of about 8 fm, and have a decaying component outside this region characterizing resonant states. Such type of states thus have a good overlap with the bound states near the Fermi surface leading to significant contribution to the pairing gap value  $\Delta_{1f_{5/2}}$ ,  $\Delta_{2p_{3/2}}$ ,  $\Delta_{2p_{1/2}}$  and also to the total pairing energy of the system near the drip-line.

In contrast, the main part of the wave function for the non-resonant states, e.g.  $1g_{9/2}$ , is seen to be spread over outside the potential region, though a small part is also contained inside the potential range. This type of state thus has a poorer overlap with the bound states near the Fermi surface leading to small value for the pairing gap  $\Delta_{1g_{9/2}}$ . Similarly, other positive energy states lying away from the Fermi level, for example,  $1h_{11/2}$ ,  $1i_{13/2}$  etc. have a negligible contribution to the total pairing energy of the system. These features can be seen from Fig. 3 which depicts the calculated pairing gap energy  $\Delta_j$  for some of the proton states in the nucleus  $^{58}_{30}\text{Zn}_{28}$ . However, we have not shown in the figure the single particle states having negligibly small  $\Delta_j$  values as these do not contribute significantly to the total pairing energy.

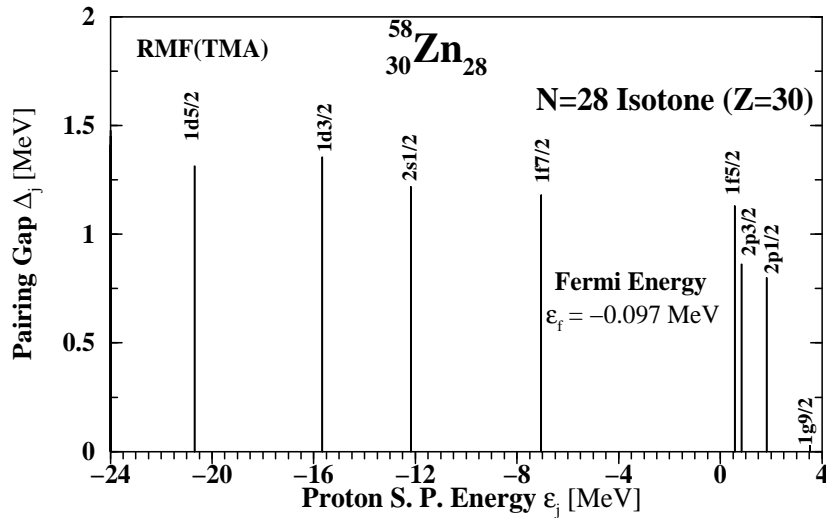


Fig. 3. Pairing gap energy  $\Delta_j$  of proton single particle states with energy close to the Fermi surface for the nucleus  $^{58}_{30}\text{Zn}_{28}$ . The resonant  $1f_{5/2}$ ,  $2p_{3/2}$  and  $2p_{1/2}$  states at energy 0.57, 0.84 and 1.82 MeV, respectively, have the gap energy of about 1 MeV which is close to that of bound states like  $1f_{7/2}$ ,  $2s_{1/2}$  etc.

One observes indeed in Fig. 3 that the gap energy for the  $1f_{5/2}$  state has a value close to 1 MeV which is quantitatively similar to that of bound states  $1f_{7/2}$  and  $2s_{1/2}$ . Also, Fig. 3 shows that the pairing gap value for the non-resonant states in the continuum, like  $1g_{9/2}$ , have negligible gap energy close to zero. On further addition



of two protons to the drip-line nucleus  ${}^{58}_{30}\text{Zn}_{28}$ , it yields the heavier isotone  ${}^{60}_{32}\text{Ge}_{28}$ . This nucleus  ${}^{60}_{32}\text{Ge}_{28}$  has negative two proton separation energy and lies beyond the proton drip-line and it is a good candidate of two proton decay as observed in Ref. 43. This nucleus decays by emission of two proton with the combined effect of the Coulomb and centrifugal barrier as has been discussed elaborately in Ref. 30. This is in contrast to the proton magic nuclei which are neutron-rich nuclei and lie near the neutron drip-line, for example the heavier isotopes of Ca <sup>28,29</sup>. As explained in Ref. 29, on further addition of neutrons in the case of neutron-rich Ca isotopes the single particle states like  $3s_{1/2}$ ,  $1g_{9/2}$  and  $2d_{5/2}$  which lie near the Fermi level gradually come down close to zero energy on increasing no. of neutrons. Even the  $1g_{9/2}$  and  $3s_{1/2}$  states become bound states. This helps in accommodating more and more neutrons which are just bound. In fact, the occupancy (no. of particle in the state) of the  $3s_{1/2}$  state in these extremely neutron-rich isotopes causes the halo formation <sup>29</sup>. This difference between the neutron-rich isotopes, and proton-rich isotones involving similar single particle states is solely caused by the large repulsive Coulomb interaction with further addition of protons. This is easily demonstrated by comparing the situations, for example, in the heavier Ca isotopes like  ${}^{62-72}\text{Ca}$  <sup>29</sup>, with that in the heavier  $N=28$  isotones like  ${}^{58}_{30}\text{Zn}_{28}$  and  ${}^{60}_{32}\text{Ge}_{28}$ .

RMF calculations <sup>32</sup> show that this nucleus  ${}^{60}_{32}\text{Ge}_{28}$  has two proton separation energy  $S_{2p} = -0.52$  and one proton separation energy  $S_p = 0.27$  and may be a possible candidate of two proton radioactivity <sup>43</sup> due to the combined barrier provided by the Coulomb and centrifugal effects. The physical situation of proton-rich  ${}^{60}_{32}\text{Ge}_{28}$  nucleus is similar to the previous nucleus  ${}^{58}_{30}\text{Zn}_{28}$ . The states  $1f_{5/2}$ ,  $2p_{3/2}$  and  $2p_{1/2}$  at energy 0.74, 1.13 and 2.12 MeV, respectively are resonant states for this nucleus. Such nuclei close to the drip-line or even beyond the drip-line have been the focus of experimental studies during the last few years employing the latest new technological advancements in the field of radioactive ion beams. Such nuclei may be good candidates of two proton radioactivity which is experimentally verified recently in the decay of  ${}^{45}\text{Fe}$  <sup>44,45</sup>, and subsequently in other experiments in the decay of  ${}^{54}\text{Zn}$  <sup>46,47</sup> and  ${}^{48}\text{Ni}$  <sup>48,49</sup>. RMF description of such nuclei has been presented elaborately in Ref. 30.

### 3.1.2. Two proton separation energy, Single particle energy:

The contribution of pairing energy plays an important role for the stability of the nuclei near the drip-lines and consequently in deciding the position of the neutron and proton drip-lines. The proton shell closure as indicated by the calculated results for  $Z = 20$  and  $28$  along with the neutron shell closure for the isotones with  $N = 28$  render the nuclei  ${}^{48}\text{Ca}$  and  ${}^{56}\text{Ni}$  doubly magic. However, it is found that the  $N = 28$  shell closure gets weakened in the proton deficient side and at  $Z = 12$  for the nucleus  ${}^{40}\text{Mg}$  the shell closure  $N = 28$  quenches which is in accordance with recent study of disappearance of  $N = 28$  magicity near drip-line <sup>35</sup>.

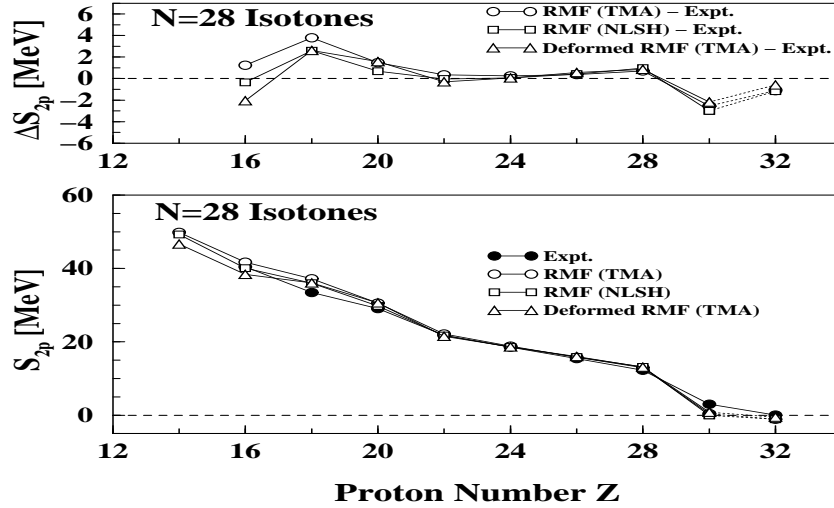
10 *G. Saxena, D. Singh, M. Kaushik, H. L. Yadav and H. Toki*

Fig. 4. Lower Panel: Two proton separation energy  $S_{2p}$  for the nuclei of  $N = 28$  isotonic chain. Spherical RMF+BCS calculations carried out with the TMA and NL-SH force parameters are compared with the available experimental data and with the deformed RMF+BCS calculations using the TMA force parametrization. Upper Panel: The difference  $\Delta S_{2p}$  of the calculated results for the two proton separation energy with respect to that of the available experimental data.

The shell structure as revealed by the pairing energies are also exhibited in the variation of two proton separation energies  $S_{2p}$  as shown in the lower panel of Fig. 4 for the  $N = 28$  isotones. It is observed from the lower panel of the figure that the spherical RMF+BCS calculations employing the TMA and NL-SH force parametrization are similar in nature, which in turn are also seen to be close to the deformed RMF+BCS calculations. A comparison of these three calculations with the available experimental data for the two proton separation energy shows that these are in fairly good agreement with the measurements. However, For the purpose of a closer comparison, we have explicitly displayed in the upper panel of Fig. 4 the differences  $\Delta S_{2p}$  between the calculated results and the experimental data for the two-proton separation energy. It is observed that the absolute value of the difference as expressed by  $\Delta S_{2p}$  varies from a minimum of close to zero, to a maximum of about 4 MeV for the entire chain of  $N = 28$  isotonic nuclei.

Furthermore, as expected, it is observed from the lower panel of Fig. 4 that an abrupt decrease in the two proton separation energy  $S_{2p}$ , occurs for the isotone lying next to a magic number. Once again this supports robust shell closures at  $Z = 20$  and  $28$  as can be seen from the lower panel of Fig. 4. Also, from this figure it is clearly seen that for the spherical as well as for the deformed RMF+BCS calculations the two proton drip-line lies at  $Z = 30$ . The  $S_{2p}$  value at the drip-line for the spherical as well as deformed RMF+BCS calculation using TMA force parameters is found to be positive. Beyond  $Z = 30$ , the  $S_{2p}$  value becomes negative

as can be seen from the lower panel of Fig. 4.

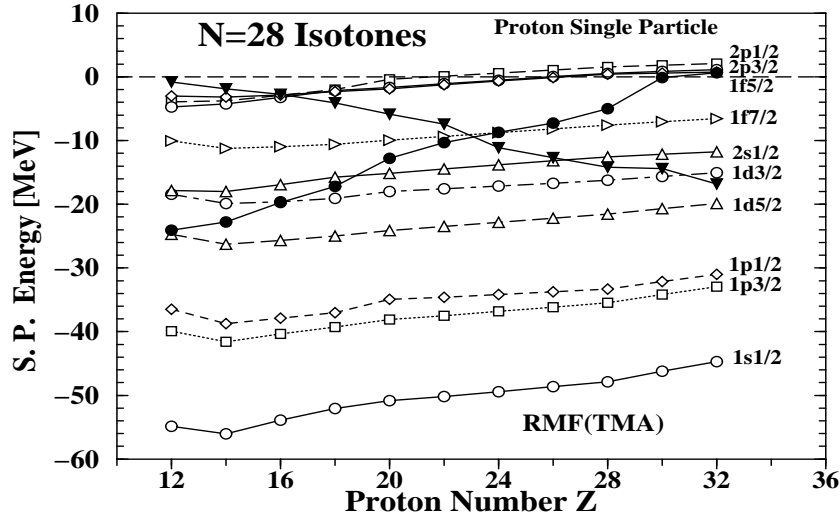


Fig. 5. Variation of the proton single particle energies obtained in the spherical RMF+BCS calculations with the TMA force for the  $N = 28$  isotones with increasing proton number. The proton Fermi level has been shown by filled circles connected by solid line, while the neutron Fermi level is depicted by filled inverted triangles also connected by solid line to guide the eyes.

In the spherical cases the structure of proton (or neutron) single particle energy and its variation with increasing proton (or neutron) number for the nuclei in general plays an important role in the understanding and explanation of position of drip-lines, variation in the proton or neutron radii and density distributions. Thus for the isotope  $^{56}_{28}\text{Ni}_{28}$  the proton and neutron single particle structures indicate shell closures for both proton and neutron due to a large gap between the single particle state  $1f_{7/2}$  and the next high lying states  $1f_{5/2}$  and  $2p_{3/2}$ . In the case of proton single particle states this gap is of about 8 MeV as can be seen in Fig. 5. Similar gap, though slightly less pronounced, between the proton single particle state  $2s_{1/2}$  and the next high lying  $1f_{7/2}$  state gives rise to shell closures at proton number  $Z = 20$  as is clearly seen in Fig. 5. Thus, the isotope  $^{48}_{20}\text{Ca}_{28}$  is seen to be a doubly magic nucleus. A large energy gap is also seen between the  $1d_{5/2}$  and  $1d_{3/2}$  proton single particle states and the proton number  $Z = 14$  is expected to produce shell closure.

From Fig. 5 it is observed that beyond the proton number  $Z = 28$ , the proton single particle states  $1f_{5/2}$  and  $2p_{3/2}$  lie in the continuum having energy 0.57 MeV and 0.84 MeV, respectively. The proton Fermi energy shown by the filled circles connected by the solid line also moves up to be very close to zero energy value ( $\epsilon_f = -0.097$  MeV). Consequently, further addition of 2 protons beyond  $Z = 28$ , partially

12 *G. Saxena, D. Singh, M. Kaushik, H. L. Yadav and H. Toki*

fills the positive energy proton single particle states  $1f_{5/2}$  and  $2p_{3/2}$  which act as resonant states for the nucleus  $^{58}_{30}\text{Zn}_{28}$  as has been described earlier in sec. 3.1.1. The occupancy i.e. number of particles occupying the levels, of these states with increasing proton number has been shown in Fig. 6.

These resonant states are akin to the bound states having their wave functions confined within the nuclear potential region, and this helps to make the isotone  $^{58}_{30}\text{Zn}_{28}$  a bound nucleus located close to the proton drip-line. Another addition of 2 protons gives the isotone  $^{60}_{32}\text{Ge}_{28}$  wherein the occupancy of the proton single particle states  $1f_{5/2}$  and  $2p_{3/2}$  increases further as is seen in Fig. 6. However, beyond  $Z = 30$ , the proton drip-line is reached the next isotone  $^{60}_{32}\text{Ge}_{28}$  is found to be unstable against 2 proton emission as has been discussed earlier.

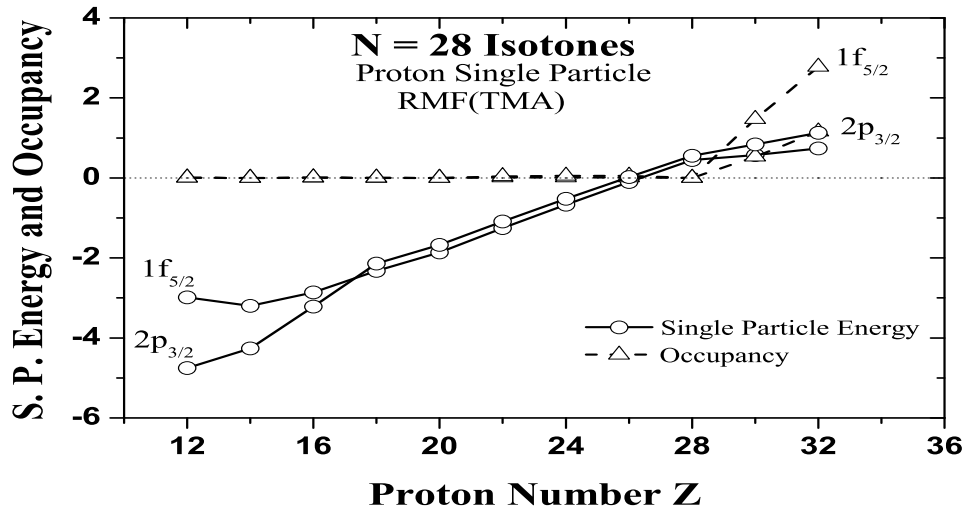


Fig. 6. Variation as a function of increasing proton number  $Z$  in energy shown by open circles, and occupancy (number of particles occupying the levels) depicted by open triangles for the proton single particle states  $1f_{5/2}$  and  $2p_{3/2}$  which act as resonant states in the proton-rich nuclei ( $Z > 28$ ) of the  $N = 28$  isotonic chain.

As remarked in previous section, even though such a nucleus is unbound its decay by 2 proton emission is appreciably delayed due to the barrier produced by the Coulomb interaction. In fact the resonant proton single particle states  $1f_{5/2}$  and  $2p_{3/2}$  could accommodate all together 10 particles beyond  $Z = 28$  and thus would have in effect pushed the proton drip-line far away to a large proton number  $Z$  instead of  $Z = 30$  in analogy, for example, to the case of Ca isotopes wherein the low lying resonant states  $1g_{9/2}$  accommodates 10 neutrons to enable the existence

of highly neutron-rich heavy Ca isotopes <sup>28,29</sup>. However, due to the disruptive Coulomb interaction amongst protons, the existence of heavier  $N = 28$  isotones beyond  $Z = 30$ , that is heavier than the isotone  ${}^{60}_{32}\text{Ge}_{28}$ , with a life time large enough to enable experimental measurements as in the case of unbound  ${}^{60}_{32}\text{Ge}_{28}$  isotone becomes rather difficult.

### **3.2. Neutron Magic Nuclei of $N = 8, 20, 40, 50, 82$ and $126$ Isotonic Chains**

In the present section it is shown that the neutron magic isotones with neutron number  $N = 8, 20, 50, 82$  and  $126$ , as well as the submagic isotones corresponding to  $N = 40$  exhibit many characteristics in common to each other and also to that of  $N = 28$  isotones. Thus, in order to save space, here we have described collectively together, though in brief, the results for the nuclei forming the isotonic chains with neutron magic and submagic numbers. Again, instead of displaying the properties of nuclei in each isotonic chain separately, to save space we have considered only a specific isotone, especially the proton-rich one, from each chain for the purpose of illustration.

The deformed RMF+BCS calculations indicate that all the isotones with neutron number  $N = 8, 20, 50, 82$  and  $126$  are almost spherical with zero quadrupole deformation parameter. Thus the chains of these isotones can be conveniently described within the spherical approach. In contrast, as expected, in the case of submagic  $N = 40$  isotonic chain the proton-rich isotones for  $Z \geq 32$  are well deformed. Thus only nuclei with the spherical shape of  $N = 40$  isotonic chain have been included in the spherical RMF+BCS description along with the isotones of the chains with  $N = 8, 20, 50, 82$  and  $126$ .

Similar to the case of heavy proton-rich nuclei in the  $N = 28$  isotonic chain, the proton-rich nuclei lying close to the proton drip-line in the isotonic chain of neutron magic numbers  $N = 40$  and  $126$ , and to a lesser extent those in the isotonic chains of  $N = 50$  and  $82$ , exhibit characteristics of having proton resonant states which help in accommodating more protons giving rise to the existence of exotic proton-rich nuclei. As opposed to the case of isotones with  $N = 28, 50, 82, 126$  and  $40$ , low lying proton resonant states are not found in nuclei of the isotonic chains with  $N = 8$  and  $20$ .

With this in view, we have chosen the nuclei  ${}^{46}_{26}\text{Fe}_{20}$ ,  ${}^{96}_{46}\text{Pd}_{50}$ ,  ${}^{154}_{72}\text{Hf}_{82}$  and  ${}^{220}_{94}\text{Pu}_{126}$  as the representative examples of the proton-rich nuclei in the  $N = 20, 50, 82$  and  $126$  neutron magic isotonic chains and describe their features in detail obtained within the spherical RMF+BCS approach. This aims to elucidate the typical features of the calculated potential, single particle wave function and the pairing gap energy etc. We have not included here the description of any proton-rich isotone for  $N = 40$  since these are well deformed as mentioned above. Also, in order to save space, we have not included any proton-rich isotone with  $N = 8$  as this case is very similar to that of the proton-rich  $N = 20$  isotones.

In Fig. 7 we have plotted using solid lines the RMF potentials, a sum of scalar and vector potentials, for the representative proton-rich  ${}^{46}_{26}\text{Fe}_{20}$ ,  ${}^{96}_{46}\text{Pd}_{50}$ ,  ${}^{154}_{72}\text{Hf}_{82}$  and  ${}^{220}_{94}\text{Pu}_{126}$  nuclei mentioned above along with the spectrum for the bound proton single particle states.

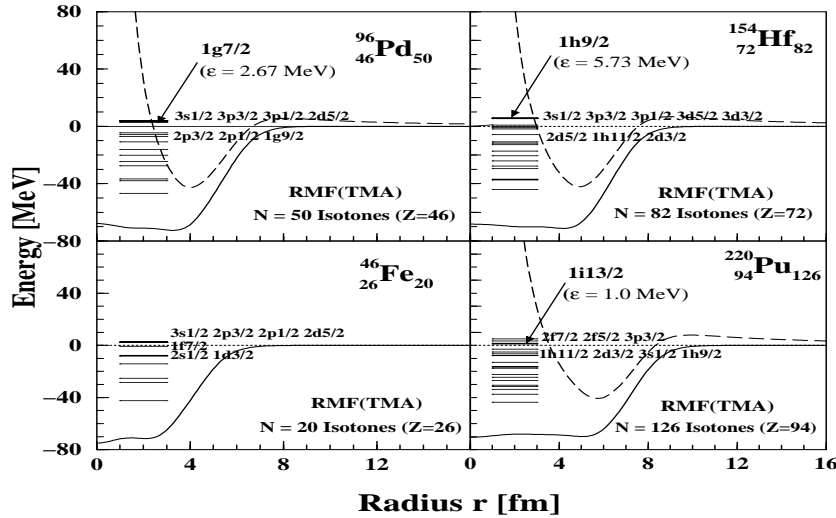


Fig. 7. The RMF potential energy plots (sum of the scalar and vector potentials) for the proton-rich  ${}^{46}_{26}\text{Fe}_{20}$ ,  ${}^{96}_{46}\text{Pd}_{50}$ ,  ${}^{154}_{72}\text{Hf}_{82}$  and  ${}^{220}_{94}\text{Pu}_{126}$  nuclei of the isotonic chain with neutron number  $N = 20, 50, 82$  and  $126$ , respectively, as a function of radius. Besides the position of low lying resonant states, the plots also show the energy spectrum of the bound and continuum proton single particle states. The long dashed line represents the sum of RMF potential energy and the centrifugal barrier energy for the proton resonant states mentioned in the plots. No low lying resonant state occurs in the case of  $N = 20$  proton-rich isotones such as  ${}^{46}_{26}\text{Fe}_{20}$ .

The plots also depict a few positive energy proton single particle states near the Fermi level, besides the low lying resonant states which contribute to the pairing energy. These resonant states are respectively,  $1g_{7/2}$  at energy  $2.67$  MeV in  ${}^{96}_{46}\text{Pd}_{50}$ ,  $1h_{9/2}$  at energy  $5.73$  MeV in  ${}^{154}_{72}\text{Hf}_{82}$  and  $1i_{13/2}$  at energy  $1.00$  MeV in  ${}^{220}_{94}\text{Pu}_{126}$ . For these resonant states we have also shown by long dashed lines the total mean-field potential given by a sum of RMF potential energy and centrifugal barrier energy. It is evident from Fig. 7 that the effective total potential for the resonant states have an appreciable barrier for the confinement of waves to form a quasi-bound state.

It is seen from Fig. 7 that with increasing proton number, as expected, the density of states increases. Moreover, with the increasing number of neutrons and protons the total RMF potential region also gets appreciably larger. Also, as described in the case of proton-rich  $N = 28$  isotonic chain nucleus  ${}^{58}_{30}\text{Zn}_{28}$ , it is evident from the plots that the effective total potential for the states  $1g_{7/2}$  in  ${}^{96}_{46}\text{Pd}_{50}$ ,  $1h_{9/2}$  in  ${}^{154}_{72}\text{Hf}_{82}$  and  $1i_{13/2}$  in  ${}^{220}_{94}\text{Pu}_{126}$  has an appreciable barrier for the confinement of

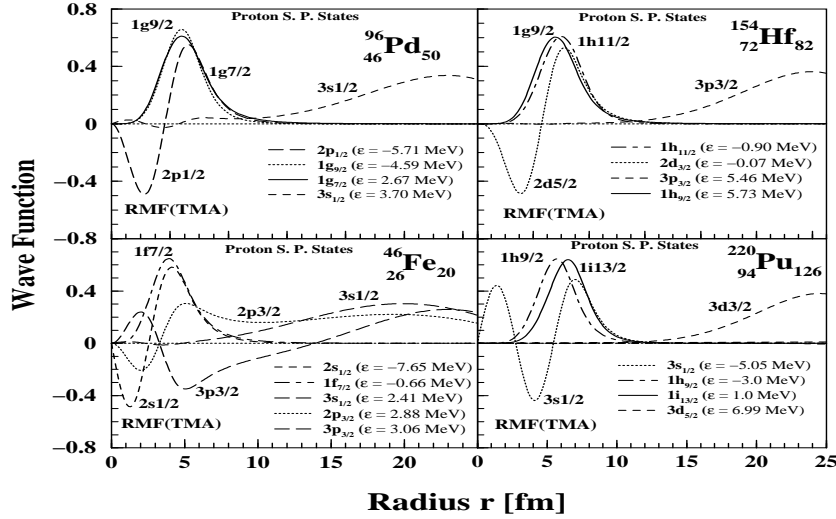


Fig. 8. Radial wave functions of a few representative proton single particle states with energy close to the Fermi surface for the proton-rich  ${}_{26}^{46}\text{Fe}_{20}$ ,  ${}_{46}^{96}\text{Pd}_{50}$ ,  ${}_{72}^{154}\text{Hf}_{82}$  and  ${}_{94}^{220}\text{Pu}_{126}$  nuclei belonging to the isotonic chains of  $N = 20, 50, 82$  and  $126$ , respectively, are shown. The proton resonant states for different nuclei have been depicted by solid lines. No low lying resonant state is found in nuclei belonging to  $N = 20$  and  $N = 8$  isotonic chains.

waves to form a quasi-bound or resonant state. The wave functions of these states exhibit characteristics similar to that of a bound state as is seen in the plots shown in Fig. 7. In contrast, the main part of the wave functions for the non-resonant states for these nuclei is seen to be mostly spread over outside their potential region. The wave function of the proton single particle states  $3s_{1/2}$  in  ${}_{26}^{46}\text{Fe}_{20}$  and  ${}_{46}^{96}\text{Pd}_{50}$ ,  $3p_{3/2}$  in  ${}_{72}^{154}\text{Hf}_{82}$ , and  $3d_{3/2}$  in  ${}_{94}^{220}\text{Pu}_{126}$  displayed in Fig. 8 represent typical examples of such states. No low lying resonant states are found in the case of proton-rich nuclei of the isotonic chains with  $N = 20$  and  $N = 8$ . For the nucleus  ${}_{26}^{46}\text{Fe}_{20}$  illustrated here as an example of proton-rich  $N = 20$  isotone, the possible proton resonant state  $1f_{5/2}$  lies much above the proton Fermi level in the continuum. Similar situation prevails for the nuclei belonging to  $N = 8$  isotonic chain. In both cases the states in the continuum close to the proton Fermi level are low angular momentum states, viz.  $3s_{1/2}$ ,  $2p_{3/2}$ ,  $2p_{1/2}$ ,  $2d_{5/2}$  etc. The effective total potential for these states does not seem to have appreciable barrier to form a quasi-bound state as is clearly seen from the wave functions of some of these states displayed in Fig. 8. The above mentioned characteristics of resonant and non-resonant states are also seen in their contributions to the pairing gap energies as has been described below.

The wave functions for the resonant states are clearly seen to be confined within a radial range of about 10 fm, and have a decaying component outside this region. Such type of states may have a good overlap with the bound states near the Fermi surface leading to significant contribution to the respective pairing gap values, and

also to the total pairing energy of the system near the drip-line.

In Fig. 9 we have displayed the pairing gap energy values of proton single particle states located close to the Fermi level. It is seen from Fig. 9 that the pairing gaps for the single particle proton states in the representative nucleus  ${}_{26}^{46}\text{Fe}_{20}$  for the isotonic chain  $N = 20$  near the Fermi level range approximately between 0.9 MeV to 1.3 MeV, where the Fermi energy lies at  $\epsilon_f = -0.041$  MeV. In contrast to other representative cases shown in Fig. 9, viz.  ${}_{46}^{96}\text{Pd}_{50}$ ,  ${}_{72}^{154}\text{Hf}_{82}$  and  ${}_{94}^{220}\text{Pu}_{126}$ , it is seen that only the lowest proton single particle states are occupied according to the number of protons, and the pairing interaction does not couple the bound states near the Fermi level with the positive energy states. Thus in the case of proton-rich  ${}_{26}^{46}\text{Fe}_{20}$  nucleus the positive energy states are not populated. A similar situation is seen to prevail in the case of nuclei belonging to the isotonic chain with  $N = 8$ .

The next two plots in Fig. 9 show the pairing gap energies for the nuclei  ${}_{46}^{96}\text{Pd}_{50}$  and  ${}_{72}^{154}\text{Hf}_{82}$  representing the proton-rich examples of the isotonic chain with  $N = 50$  and  $N = 82$  respectively. Again, it is clearly seen in the figure that the resonant proton single particle states  $1g_{7/2}$  ( $\epsilon = 2.67$  MeV) in  ${}_{46}^{96}\text{Pd}_{50}$  and  $1h_{9/2}$  ( $\epsilon = 5.73$  MeV) in  ${}_{72}^{154}\text{Hf}_{82}$  have large pairing gap values similar to that of bound proton single particle states. These resonant states lie far away from the proton Fermi level which is located at  $\epsilon_f = -4.11$  MeV in  ${}_{46}^{96}\text{Pd}_{50}$  and at  $\epsilon_f = -0.487$  MeV in  ${}_{72}^{154}\text{Hf}_{82}$ . Due to such energy difference the resonant states in these nuclei are not able to connect to the states near the Fermi level through the pairing correlations and, therefore, their contribution to the pairing energy is also rather small. This also implies that the effect of resonant states in accommodating more protons to the system near the proton drip-line, and hence pushing the drip-line further is not prominent in the case of  ${}_{46}^{96}\text{Pd}_{50}$  and  ${}_{72}^{154}\text{Hf}_{82}$  nuclei of the isotonic chains with  $N = 50$  and  $N = 82$ .

For the nucleus  ${}_{94}^{220}\text{Pu}_{126}$  representing the isotonic chain with neutron number  $N = 126$  the proton single particle resonant state is  $1i_{13/2}$  as shown in Fig. 9. This resonant state lies at energy  $\epsilon = 1.00$  MeV, whereas the proton Fermi level is located at  $\epsilon_f = -0.149$  MeV. Again, it is seen that the pairing gap energy of the resonant  $1i_{13/2}$  state has a value  $\Delta_j \approx 1.2$  MeV, which is close to that of the bound states.

As can be seen in the plot for the  ${}_{94}^{220}\text{Pu}_{126}$  isotone in Fig. 9, there are other continuum states, viz.  $2f_{7/2}$ ,  $2f_{7/2}$ ,  $3p_{3/2}$ ,  $3p_{3/2}$  and  $1i_{11/2}$  which lie at higher energy and have relatively appreciable values for the pairing gap energy. The proton  $1i_{13/2}$  state being a resonant state has good overlap with the bound states and, therefore, is found to have sizeable contribution to the pairing energy. This helps in the occurrence of bound proton-rich isotone  ${}_{94}^{220}\text{Pu}_{126}$  located at the two proton drip-line for the  $N = 126$  isotonic chain. Other states mentioned above; though these also have appreciable pairing gap energy, are found to have no substantial overlap with the bound states lying far down in energy. This implies that the occupancy of these continuum states is negligible and their contribution to the total pairing energy is not substantial. Contrary to this, the resonant single particle state  $1i_{13/2}$



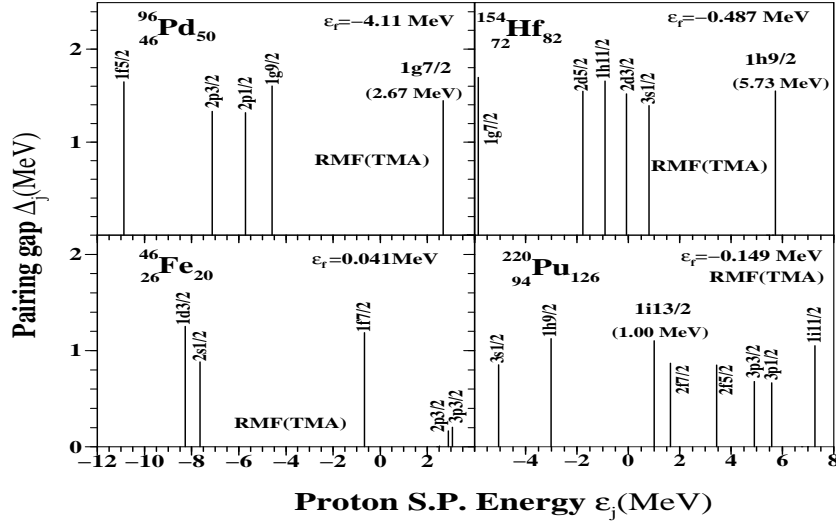


Fig. 9. Pairing gap energy  $\Delta_j$  of proton single particle states with energy close to Fermi level for the proton-rich nuclei  $^{46}_{26}\text{Fe}_{20}$ ,  $^{96}_{46}\text{Pd}_{50}$ ,  $^{154}_{72}\text{Hf}_{82}$  and  $^{220}_{94}\text{Pu}_{126}$  representing the isotonic chains with  $N = 20, 50, 82$  and  $126$ , respectively.

is found to be filled in by  $\approx 2$  protons.

#### 4. Summary

In the present investigations we have employed relativistic mean-field plus BCS (RMF + BCS) approach<sup>14,16,17,18,19,20,23,24,28,30,31,32</sup> to carry out a systematic study for the ground state properties of the entire chains of even-even neutron magic nuclei represented by isotones of traditional neutron magic numbers  $N = 8, 20, 28, 50, 82$  and  $126$  as well as isotones of  $N = 40$ , considered to be neutron sub-magic. From the extensive calculations it is established that the majority of isotones belonging to these chains are indeed spherical. For this purpose we have employed the deformed RMF+BCS approach wherein for the sake of simplicity only axially deformed shapes are considered<sup>19,20,24</sup>. For our calculations in both approaches, the deformed RMF+BCS and the spherical RMF+BCS, we have used the TMA<sup>23</sup> Lagrangian density extensively used in the relativistic mean-field calculations<sup>28,29,32</sup>. Further, in order to check the validity of our description for different RMF force parameterizations, we have carried out the spherical RMF+BCS calculations using also the NL-SH<sup>24,25</sup> Lagrangian density which has been equally popular for the relativistic mean-field calculations.

One of the prime reason of this study has been to look into the role of low lying resonant states which have been found earlier in the investigations of proton magic isotopes of nuclei<sup>28,29</sup> to act akin to the bound states leading to accumulation of additional loosely bound neutrons. Eventually this resulted in the existence of

highly neutron-rich nuclei. In some cases, even the occurrence of halo formation, for example in the heavy Ca and Zr isotopes, has been predicted<sup>28,29</sup>. It is found that the same mechanism does persist in these neutron magic nuclei and the proton single particle resonant states play the same role here and give extra stability to drip-line nucleus (nuclei). However, the phenomenon gets restricted to the accumulation of only a few protons due to the disruptive Coulomb forces amongst protons.

As an important result of the present studies we have described the effect of proton single particle resonant states in accommodating additional protons, which results effectively in extending the two proton drip-line. This has been illustrated through the example of proton-rich isotope  ${}^{58}_{30}\text{Zn}_{28}$  lying at the two proton drip-line of the  $N = 28$  isotonic chain. Similar to the case of heavy proton-rich nuclei in the  $N = 28$  isotonic chain, the proton-rich nuclei lying close to the proton drip-line in the isotonic chain of neutron magic numbers  $N = 40$  and 126, and to a lesser extent those in the isotonic chains of  $N = 50$  and 82, exhibit characteristics of having proton resonant states which help in accommodating more protons giving rise to the existence of exotic proton-rich nuclei. Towards this end, we have chosen for the purpose of illustration the isotones  ${}^{46}_{26}\text{Fe}_{20}$ ,  ${}^{96}_{46}\text{Pd}_{50}$ ,  ${}^{154}_{72}\text{Hf}_{82}$  and  ${}^{220}_{94}\text{Pu}_{126}$  as the representative examples of the proton-rich nuclei in the  $N = 20, 50, 82$  and 126 neutron magic isotonic chains.

It is found for all the isotonic chains considered in the present study that the calculated binding energy values obtained by employing the deformed RMF+BCS approach are in very good agreement with the available experimental data<sup>50</sup>. Since majority of the isotones described here are spherical, these results are obviously also in accord with the spherical RMF+BCS calculations as in the case of the  $N = 28$  isotonic chain. Moreover, results of our spherical RMF+BCS calculations using TMA and NL-SH force parameters produce similar results. This similarity in results is seen to hold true for all the other physical quantities, viz. the rms radii and densities for proton and neutron distributions etc. indicating the force independence of these results.

### Acknowledgements

Support through a grant (SR/S2/HEP-01/2004) by the Department of Science and Technology (DST), India, is acknowledged. The authors are indebted to Dr. L. S. Geng, RCNP, Osaka University, Osaka, Japan, for valuable correspondence.

### References

1. I. Tanihata, *J. Phys. G* **22** (1996) 157.
2. Rituparna Kanungo, I. Tanihata and A. Ozawa, *Phys. Lett. B* **512** (2001) 261.
3. A. Ozawa, T. Kobayashi, T. Suzuki, K. Yoshida and I. Tanihata, *Phys. Rev. Lett.* **84** (2000) 5493.
4. A. Ozawa *et al.*, *Nucl. Phys. A* **709** (2002) 60.
5. C. B. Hinke *et al.*, *Nature* **486** (2012) 341.
6. R. Kanungo *et al.*, *Phys. Rev. Lett.* **102** (2009) 152501.

7. K. Tanaka et al., *Phys. Rev. Lett.* **104** (2010) 62701.
8. J. Dobaczewski, H. Flocard and J. Treiner, *Nucl. Phys. A* **422** (1984) 103.
9. K. Bennaceur, J. Dobaczewski and M. Ploszajczak, *Phys. Lett. B* **496** (2000) 154.
10. J. Terasaki, P. H. Heenen, H. Flocard and P. Bonche, *Nucl. Phys. A* **600** (1996) 371.
11. M. Grasso, N. Sandulescu, Nguyen Van Giai and R. J. Liotta, *Phys. Rev. C* **4** (2001) 064321.
12. N. Sandulescu, R. J. Liotta and R. Wyss, *Phys. Lett. B* **394** (1997) 6.
13. N. Sandulescu, Nguyen Van Giai and R. J. Liotta, *Phys. Rev. C* **61** (2000) 061301(R).
14. J. D. Walecka, *Ann. Phys. (N.Y.)* **83** (1974) 491.
15. J. Boguta, A. R. Bodmer, *Nucl. Phys. A* **292** (1977) 413.
16. B. D. Serot and J. D. Walecka, *Adv. Nucl. Phys.* **16** (1986) 1.
17. P.-G. Reinhard, M. Rufa, J. Marhun, W. Greiner and J. Friedrich, *Z. Phys. A* **323** (1986) 13.
18. P-G Reinhard, *Rep. Prog. Phys.* **52** (1989) 439.
19. Y. K. Gambhir, P. Ring and A. Thimet, *Ann. Phys. (N.Y.)* **198** (1990) 132.
20. P. Ring, Y. K. Gambhir and G. A. Lalazissis, *Comput. Phys. Commun.* **105** (1997) 77.
21. H. Toki, Y Sugahara, D. Hirata, B. V. Carlson and I. Tanihata, *Nucl. Phys. A* **524** (1991) 633.
22. D. Hirata, H. Toki, I. Tanihata and P. Ring, *Phys. Lett. B* **314** (1993) 168.
23. Y. Sugahara and H. Toki, *Nucl. Phys. A* **579** (1994) 557.
24. P. Ring, *Prog. Part. Nucl. Phys.* **37** (1996) 193.
25. M. M. Sharma, M. A. Nagarajan and P. Ring, *Phys. Lett. B* **312** (1993) 377.
26. J. Meng, P. Ring, *Phys. Rev. Lett.* **80**, (1998) 460.
27. J. Meng, H. Toki, J.Y. Zeng, S. Q. Zhang and S. Q. Zhou, *Phys. Rev. C* **65** (2002) 041302(R).
28. H. L. Yadav, S. Sugimoto and H. Toki, *Mod. Phys. Lett. A* **17** (2002) 2523.
29. H. L. Yadav, M. Kaushik and H. Toki, *Int. Jour. Mod. Phys. E* **13** (2004) 647.
30. D. Singh, G. Saxena, M. Kaushik, H. L. Yadav and H. Toki *Int. Jour. Mod. Phys. E* **21**, No. 9 (2012) 1250076.
31. G. Saxena, D. Singh, H. L. Yadav, A. Haga and H. Toki, *Mod. Phys. Lett. A* **23** (2008) 2589.
32. L. S. Geng, H. Toki and J. Meng, *Prog. Theor. Phys.* **113** (2005) 785.
33. R. Broda, B. Fornal, W. Krolas and T. Pawlat, *Phys. Rev. Lett. B* **74**, 6, (1995) 868.
34. L. S. Geng, H. Toki and J. Meng, *J.Phys. G* **30** (2004) 1915.
35. Z. P. Li, J. M. Yao, D. Vretenar, T. Niksic, H. Chen and J. Meng, *Phys. Rev. C* **84** (2011) 054304.
36. O. Sorlin, M.-G. Porquet, arXiv:1209.3377.
37. N A Smirnova, B Bally, Kristiaan Heyde UGent, F Nowacki and K Sieja, *Phys. Lett. B* **686** (2010) 109.
38. Lane A. M., "Nuclear Theory", Benjamin, (1964).
39. Ring P. and Schuck P., "The Nuclear many-body Problem", Springer , (1980).
40. Bertsch G. F. and Esbensen H., *Ann. Phys. (N.Y.)* **209** (1991) 327.
41. Migdal A. B., "Theory of Finite Fermi Systems and Applications to Atomic Nuclei," Interscience, New York, (1967).
42. D. Vautherin, *Phys. Rev. C* **7** (1973) 296.
43. A. Stolz et. al., *Phys. Lett. B* **627** (2005) 32.
44. M. Pfutzner et al., *Eur. Phys. Jour. A* **14** (2002) 279.
45. J. Giovinazzo et. al., *Phys. Rev. Lett.* **89** (2002) 102501.
46. B. Blank et. al., *Phys. Rev. Lett.* **94** (2005) 232501.

20 *G. Saxena, D. Singh, M. Kaushik, H. L. Yadav and H. Toki*

47. P. Ascher et. al., *Phys. Rev. Lett.* **107** (2011) 102502.

48. C. Dossat et. al., *Phys. Rev. C* **72** (2005) 054315.

49. M. Pomorski et. al., *Phys. Rev. C* **83** (2011) 061303.

50. G. Audi and A. H. Wapstra, *Nucl. Phys. A* **595** (1995) 409.